α- and neutron-induced reactions on ruthenium isotopes

W. Rapp,* M. Heil, D. Hentschel, F. Käppeler, and R. Reifarth
Forschungszentrum Karlsruhe, Postfach 3640, D-76021 Karlsruhe, Germany

H. J. Brede and H. Klein
Physikalisch-Technische Bundesanstalt, Bundesallee 100, D-38116 Braunschweig, Germany

T. Rauscher
Departement für Physik und Astronomie, Universität Basel, Klingelbergstrasse 82, CH-4056 Basel, Switzerland
(Received 21 December 2001; published 18 July 2002)

The uncertain origin of the proton rich Mo and Ru isotopes has motivated cross-section measurements of α- and neutron-induced reactions. The experiments were performed via the activation technique by irradiating thin layers of natural ruthenium with α-particle beams close to the Gamov window of the *p* process between 7.0 and 10.5 MeV. The cross sections of the reactions ^{96}Ru(α,γ), ^{96}Ru(α,n), ^{96}Ru(α,p), and ^{98}Ru(α,n) could be determined with uncertainties of typically 10%. On average, these results are about two to three times smaller than recent statistical model predictions. Additional activations in a quasistellar neutron spectrum corresponding to $kT=25$ keV allowed us to obtain the complementary stellar (n,γ) cross sections for ^{96}Ru, ^{102}Ru, and ^{104}Ru. In these cases the agreement with model calculations is considerably better.

DOI: 10.1103/PhysRevC.66.015803 PACS number(s): 97.10.Tk, 25.40.−h, 26.30.+k, 27.60.+j

I. INTRODUCTION

In total 32 stable isotopes between ^{74}Se and ^{196}Hg on the proton-rich side of the valley of stability witness the so-called *p* process. These *p* nuclei are shielded from beta decay of *s* or *r* process nuclides (see Fig. 1). They presumably originate from explosive burning during type II supernova explosions where sufficiently high temperatures of $2-3\times10^9$ K are reached for a time scale of a few seconds. This leads to a multitude of (γ,n), (γ,p), and (γ,α) reactions on preexisting seed nuclei. The resulting complex reaction network includes about 10 000 reactions combining several thousand mostly unstable nuclei on the proton-rich side close to the stability valley.

The *p* abundances are typically 10–100 times smaller than comparable *s* and *r* abundances. There are, however, four prominent exceptions exhibiting much larger abundances: ^{92}Mo, ^{94}Mo, ^{96}Ru, and ^{98}Ru with isotopic abundances of 14.8%, 9.2%, 5.5%, and 1.9%, respectively. Figure 1 illustrates that these nuclei are clearly separated from the reaction flows of the neutron capture scenarios related to the *s* and *r* processes, which dominate all other isotopic abundances beyond iron.

Current *p*-process models have severe problems in describing these Mo and Ru isotopes, finding significant underproduction for the case of type II supernovae [1,2] or a corresponding overproduction of the lighter *p* nuclei ^{74}Se, ^{78}Kr, and ^{84}Sr in type Ia supernovas [3]. Recently it was suggested to solve this problem by increasing the adopted rate for the ^{22}Ne(α,n) reaction by factors of 10–50 [4]. Although such a large variation would imply dramatic consequences for the well-founded *s* process and has actually been ruled out by recent data [5], it underlines the importance of accurate nuclear reaction data. An alternative explanation could be that this group of nuclei may originate from the *rp* process [6], where the termination of the reaction path was found to be located around $A\approx100$ [7]. This possibility needs to be investigated in more detail, however.

One important requirement for improving this unsatisfactory situation is to minimize the nuclear physics uncertainties, which are still obscuring the reliability of the calculated *p* abundances. Since there is no way to study any substantial fraction of the very many photodisintegration and capture reactions involved in the *p* process, practically all these rates have to be determined by comprehensive model calculations. Since any *p*-process study must rely on these theoretical reaction rates, experimental information is crucial for testing the credibility of such calculations. At present, however, this information is still very scarce for (p,γ) reactions and the situation is even worse for the reactions involving α particles. There are only two experiments directly measuring α capture at low energies, one for ^{70}Ge [8] and one for ^{144}Sm

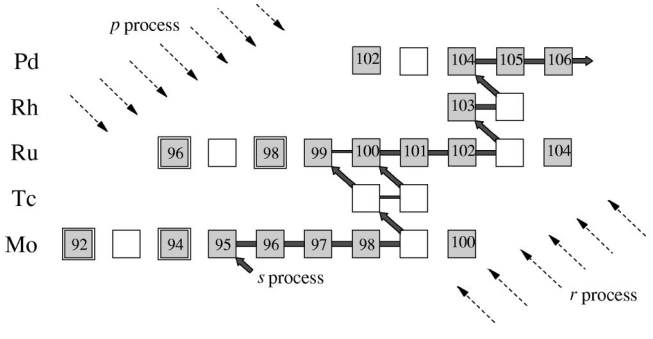

FIG. 1. The main nucleosynthesis mechanisms in the mass region between Zr and Ru are the *s* and *r* processes. Both reaction flows bypass the abundant *p* nuclei ^{92}Mo, ^{94}Mo, ^{96}Ru, and ^{98}Ru. Stable and unstable isotopes are indicated by shaded and open squares, respectively.

*Electronic address: wolfgang.rapp@ik.fzk.de

TABLE I. Experimental runs for α-induced reactions.

	Activations		Samples		
Run	α-Energy[a] (MeV)	Irradiation time (s)	XRF result (Å)	RBS result (Å)	Weighted average (10^{18} at/cm^2)
α1	10.997	2730	2832±99	2940±265	2.07±0.07
α2	10.540	2730	1488±52	1470±132	1.10±0.04
α3	10.540	2730	3016±106	3110±280	2.21±0.08
α4	10.228	2730	2934±103	2930±264	2.17±0.08
α5	10.120	16230	913±32	914±82	0.675±0.024
α6	10.12	1230	831±29	883±79	0.606±0.022
α7	9.694	2730	2883±101	2940±265	2.12±0.08
α8	9.400	14400	882±31	880±79	0.652±0.023
α9	8.900	32490	1549±54	1480±133	1.16±0.04
α10	8.500	64860	2986±104	3040±274	2.20±0.08
α11	7.987	50940	4042±141	4150±374	2.97±0.11
α12	7.322	84660	5079±178	5180±466	3.74±0.13

[a]Uncertainty 25 keV.

[9,10]. In another experiment, the reaction ^{147}Sm(n,α) was studied in order to test the sensitivity of the α channel [11].

This need for experimental cross sections of direct or inverse reaction rates motivated a series of experiments at the Karlsruhe Van de Graaff accelerator, which were focussed on the mass region of the Mo and Ru isotopes. First results on stellar (p,γ) rates of ^{92,94,95,98}Mo [12] and ^{96,98,99,104}Ru [13] are complemented by the present work on α-induced reactions. Such data are particularly important, not only because there are almost no data for these cross-sections at astrophysically relevant energies, but because the result for the ^{144}Sm(α,γ) rate was found to be an order of magnitude smaller than theoretical predictions [9]. In the light of this discrepancy, it was interesting whether the difficulty in explaining the puzzling p abundances of ^{96,98}Ru and ^{92,94}Mo could be related to similar discrepancies in the reaction rates or whether the severe ^{144}Sm discrepancy was just a local problem.

The present work describes cross section measurements of α- and neutron-induced reactions on ^{96}Ru, ^{102}Ru, and ^{104}Ru [14]. All measurements have been carried out via the activation technique using α energies between 7.0 and 10.5 MeV, in the or near the Gamov window of the p process (which corresponds to α energies from 4.6 to 10.2 MeV for temperatures between 1.8×10^9 and 3.3×10^9 °C), and a quasistellar neutron spectrum for 25 keV thermal energy (Secs. II–IV). The deduced cross sections presented in Sec. V are compared with theoretical data obtained with the statistical model code NON-SMOKER [15], followed by a summary in Sec. VI.

II. MEASUREMENTS

The cross-section measurements described in this work were performed with the activation technique. For the α-induced reactions thin samples were irradiated and analyzed following the method developed previously for a series of (p,γ) reactions [12,13], whereas the neutron cross sections were obtained using the standard technique described in Refs. [16,17].

A. Target preparation

The two types of activations required rather different samples, i.e. thin Ru layers on tungsten backings for the α-induced reactions and comparably thick Ru foils for the neutron capture measurements.

For the α-induced reactions the target thickness represents a compromise between the need for sufficient counting statistics and an acceptable energy spread. In order to control the related systematic effects, targets were prepared for a thickness range between 80 and 600 nm, corresponding to α-energy losses between 50 and 600 keV in the investigated energy range [18]. Metallic Ru layers of 10 mm diameter were sputtered onto 1 mm thick tungsten substrates of 35 mm diameter in an argon atmosphere of 6.4×10^{-2} mbar [13]. Parasitic activities from target contaminations were minimized by using tungsten of 99.996% purity. During the sputtering process the substrates were heated to ≈90 °C to improve the stability and homogeneity of the Ru layers. The resulting thickness was controlled via the sputter time and was determined for each target by two independent methods, Rutherford backscattering (RBS) and x-ray fluorescence analysis (XRF). The relevant targets used in the activations are listed in Table I.

In addition, a series of Ru layers on carbon substrates was produced for more sensitive RBS studies. Apart from Ru, the only impurity identified in these RBS spectra was an oxygen contamination of ≈16%. However, this component did not affect the later activations because of the very short half-lives of the corresponding reaction products.

For the (n,γ) reactions a set of samples was prepared from Ru metal of 99.9% purity. The foils were 6, 8, 10 mm in diameter and 0.2 mm or 1 mm thick. The use of different sample parameters allowed to investigate systematic uncertainties and to verify the respective corrections applied in data analysis by direct comparison of the corresponding

TABLE II. Sample combinations for (n,γ) reactions.

Run	Ru sample			Au samples	
	Thickness (mm)	Diameter (mm)	(10^{20} at/cm^2)	Front[a] (10^{20} at/cm^2)	Back[a] (10^{20} at/cm^2)
$n1$	1	6	65.15 ± 0.22	1.776 ± 0.004	1.756 ± 0.004
$n2$	1	8	64.82 ± 0.16	1.768 ± 0.003	1.804 ± 0.003
$n3$	1	10	64.66 ± 0.13	1.789 ± 0.002	1.774 ± 0.002
$n4$	0.2	6	11.04 ± 0.04	1.803 ± 0.004	1.749 ± 0.004
$n5$	0.2	8	12.54 ± 0.03	1.780 ± 0.003	1.800 ± 0.003
$n6$	0.2	10	13.96 ± 0.03	1.749 ± 0.002	1.746 ± 0.002

[a]As seen from neutron target.

cross-section results. The cross sections were determined relative to the standard cross section of ^{197}Au by irradiating thin gold foils together with the Ru samples. Each sample sandwich was accurately centered on a thin KAPTON foil stretched over an aluminum ring for exact positioning during the irradiation as well as during the subsequent measurement of the induced activities. The sample parameters are given in Table II.

B. Characterization of samples

The thickness for the targets for the α-induced reactions was determined by XRF and by Rutherford backscattering. XRF analyses were carried out with a Siemens SRS 3000 crystal spectrometer that was operated with a rhodium anode and a LiF crystal for analyzing the induced characteristic x rays. The efficiency of the spectrometer was calibrated by means of 11 well-defined samples prepared from a standard Ru solution. In this way the samples could be characterized with an accuracy of $\pm3.5\%$.

The additional RBS analyses were somewhat hampered by backscattering from the tungsten backing, which obscured the expected peak from the Ru layers as shown in Fig. 2. Therefore, the thickness of the Ru layers had to be inferred from the position of the W edge in the spectrum rather than from the Ru signal itself, yielding somewhat larger uncertainties of $\pm7.5\%$. The RBS spectra were analyzed using the RUMP code [19] including the (small) effect of the oxygen impurity. The XRF and the RBS results being in good agreement (Table I), the weighted average was adopted in further data analysis.

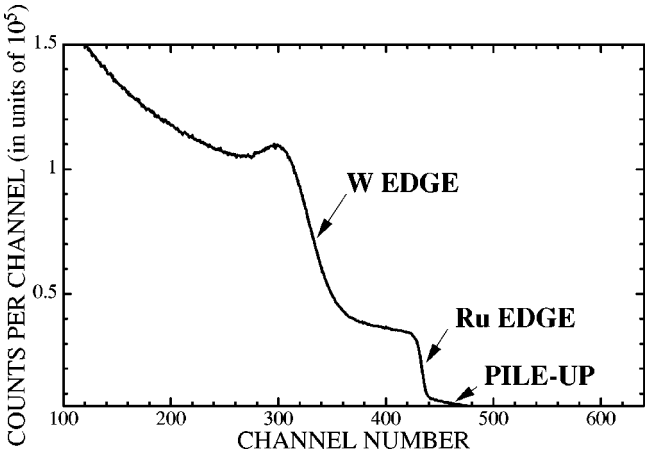

FIG. 2. RBS spectrum of a Ru sample taken with an α energy of 2 MeV. The shift of the tungsten edge due to the energy loss in the Ru layer yields a target thickness of 3600 Å.

The much thicker samples for the neutron induced reactions could be accurately defined by the weight of the Au and Ru foils as given in Table II.

C. Detector calibration

In both experiments, the induced activities were counted off line with calibrated high purity germanium (HPGe) detectors. Since the α irradiations were carried out in subsequent runs, two such detectors with active volumes of 263 and 173 cm^3 (corresponding to 65% and 35% relative efficiency) were used in parallel setups. Because of the rather small induced activities, a close counting geometry had to be chosen.

In order to determine the counting efficiency in close geometry and to assess the sensitivity of the sample-detector position, the setup was simulated with the GEANT 3.1 package. These studies led us to choose a distance of 11 mm between sample and the entrance window of the HPGe detectors. The sample position was exactly defined by holders that were adapted to the detector dimensions. Counting in close geometry implies sizable corrections for summing-in or summing-out effects, since cascade γ rays and the related x rays may well be detected in coincidence. The respective corrections for the investigated reactions will be discussed in Sec. IV. Natural γ background was reduced to 15 events per s in the energy range $E_\gamma<1$ MeV by means of a 5 cm thick lead shield with 5.5 mm thick Cu to absorb residual Pb x rays.

The detector efficiencies were measured with weak γ sources in order to minimize corrections for pile up and dead time. The measurements were carried by using single-line decays, i.e., ^{241}Am (59.5 keV), ^{109}Cd (88.0 keV), ^{137}Cs (661.7 keV), ^{65}Zn (1115.0 keV), as well as γ cascades from ^{57}Co (122.1–136.5 keV), and ^{113}Sn (255.1–391.7 keV). The latter were used to verify the summing effects obtained in Monte Carlo simulations with the CASC code [20]. As shown in Fig. 3 for the larger HPGe detector, absolute efficiencies between 2% and 20% could be achieved in the relevant energy range. The uncertainties of the experimental points were between 2% and 3%, comparable to the size of the black dots in Fig. 3. These results were complemented by GEANT simu-

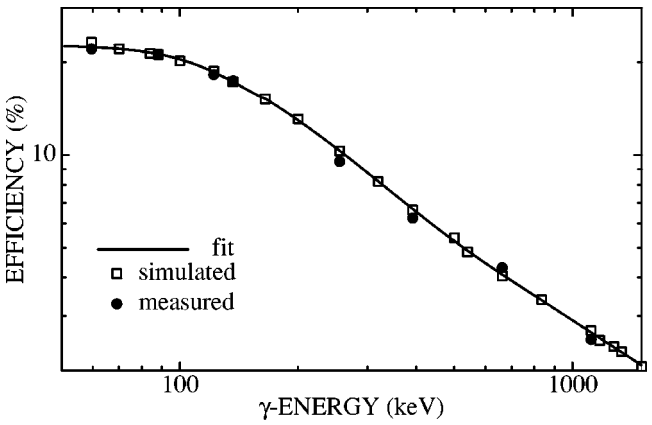

FIG. 3. The absolute efficiency of the 263 cm^3 HPGe detectors was measured with calibrated sources (black circles). These values were complemented by GEANT simulations (open squares), which were found in good agreement with the experimental results. The fit to both data sets (solid curve) was adopted in analyzing the induced γ activities from the α and neutron irradiations.

lations, which were found in good agreement with the measured data. In further analyses, the γ efficiency was represented by a fit to both data sets (solid line). Corresponding to the scatter of data points around the fit an overall uncertainty of 3% was adopted for the close geometry necessary for the low α-induced activities.

In the neutron irradiations significantly higher activities were to be expected. Accordingly, a smaller HPGe detector of 39 cm^3 and a wider counting geometry with negligible corrections for pile up and dead time effects could be used. For the adopted sample positions 20.6 cm and 7.3 cm from the detector window, the γ efficieny was measured to an accuracy of 2% using a set of calibrated sources including ^{241}Am (59.5 keV), ^{109}Cd (88.0 keV), ^{137}Cs (661.7 keV), ^{54}Mg (834.8 keV), ^{57}Co (122.1 keV; 136.5 keV), ^{113}Sn (255.1 keV; 391.7 keV), and ^{60}Co (1173.2 keV; 1332.5 keV). Because of its smaller size the natural background of this detector was only 1.4 events per s in the energy interval between 200 and 800 keV.

III. ACTIVATION EXPERIMENTS

A. Alpha-induced reactions

The cross sections were measured at the cyclotron of the Physikalisch Technische Bundesanstalt Braunschweig (PTB). In total, 12 activations were performed covering the energy range $7.0 < E_\alpha < 10.6$ MeV. Before each activation, the α energy was determined to ± 25 keV by two 90° analyzing magnets. For the irradiations, the beam line was opened in front of the first analyzing magnet for installing the target chamber with the water-cooled samples as sketched in Fig. 4. During the irradiations the beam was defocussed to reduce the thermal load on the targets. The diameter of the beam was defined to 9 mm by a cooled diaphragm. The target chamber was designed as a Faraday cup to ensure the accurate registration of the beam current. The emission of secondary electrons from the target was suppressed by a bias voltage of -90 V. Throughout the irradiations the current of typically

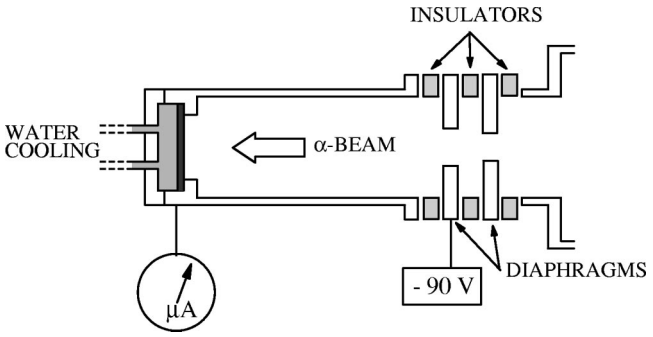

FIG. 4. Activation scheme at the PTB cyclotron. The sketch indicates the energy calibration of the α beam by two 90° magnets and the irradiation position.

11–15 μA was recorded with a digital integrator in time steps of 30 s for proper off-line correction of the decays during the irradiations.

According to the steeply decreasing cross section, irradiation times between 12 min and 24 h had to be chosen. In the longer irradiations below 9 MeV α energy the samples developed blisters due to the extended α bombardment. But since the blisters did not break open, these runs could be evaluated via the induced γ activity without further corrections. The activity measurements were carried out with calibrated HPGe detectors of 263 cm^3 and 173 cm^3.

B. Neutron-induced reactions

The (n,γ) activations were carried out at the Karlsruhe Van de Graaff accelerator. Neutrons were produced via the ^{7}Li$(p,n)^7$Be reaction by bombarding metallic Li layers evaporated onto 1 mm thick copper backings. The neutron spectrum obtained with a proton energy 30 keV above the reaction threshold at 1881 keV corresponds to a quasistellar Maxwell-Boltzmann distribution with a thermal energy $kT = 25$ keV [16,21]. Under these conditions, all neutrons are emitted in a forward cone of 120° opening angle (Fig. 5). Before each activation the proton energy was adjusted by a neutron time-of-flight measurement with the accelerator operated in pulsed mode (repetition rate 1 MHz, pulse width 15 ns) in order to verify that the energy of the fastest neutrons were properly adjusted to $E_n = 106$ keV.

In total, six activations of about 1 h were carried out with a proton beam current of 100 μA producing a fluence of 10^9 neutrons per s. During the irradiations, the neutron yield was continuously monitored in 1 min intervals by means of a ^{6}Li-glass detector for off-line corrections of the decays during the irradiations. The samples were sandwiched between gold foils and placed directly at the neutron target (Fig. 5). Systematic uncertainties were studied by variation of sample diameter and thickness.

The induced γ activities were measured with the 39 cm^3 HPGe detector as described below.

IV. DATA ANALYSIS

The unstable nuclei produced by the investigated α- and n-induced reactions are illustrated at the example of ^{96}Ru in

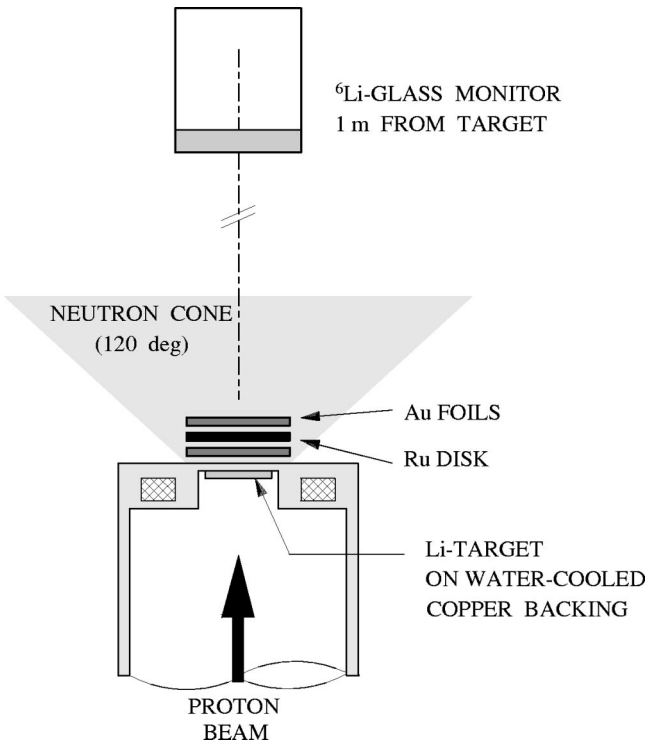

FIG. 5. Setup for the neutron irradiations at the Karlsruhe Van de Graaff accelerator.

Fig. 6. The induced activties can always be attributed to a specific reaction, except for ^{96}Ru. In this case the contribution of the (α,n) channel interferes with the ^{99}Rh activity produced by (α,p) reactions.

A. Alpha-induced reactions

The time evolution of the respective abundances $X(t)$ can be described by a production and a destruction term

$$\frac{dX(t)}{dt}=\sigma_x\Phi(t)N_0-\lambda_x X(t), \tag{1}$$

where the production is determined by the respective cross section σ, the projectile flux Φ, and the atom densities of the samples N_0, while the destruction is characterized by the decay constants λ. For constant projectile flux this leads to the solution

$$X(t)=\sigma_X\Phi N_0\frac{1-e^{-\lambda_X t}}{\lambda_X}. \tag{2}$$

In reality, unavoidable fluctuations of the particle flux require numerical integration of Eq. (1) over the experimentally recorded time intervals Δt, in which the particle flux can be assumed to be constant (see Ref. [12]).

The above equations had to be modified for reactions, where the induced activity was affected by an interfering channel and/or by the population of a relevant isomer. For example, the activity produced by the ^{96}Ru$(\alpha,p)^{99}$Rh reaction had to be corrected for the ^{99}Pd decays to the isomer in ^{99}Rh, which results from the competing (α,n) channel. In that case, the isomer in ^{99}Rh does not decay to the ground state and can, therefore, be treated as an independent isotope. Accordingly, one finds

$$\frac{dY(t)}{dt}=-\lambda_Y Y(t)+\vartheta\lambda_X X(t)+\sigma_Y\Phi(t)N_0, \tag{3}$$

where the decay branch to the isomer in ^{99}Rh is expressed by ϑ. The number of decays during the counting time t_m becomes

$$A_Y=Y(t_a)(1-e^{-\lambda_Y t_m})e^{-\lambda t_w}+\frac{\vartheta\lambda_X\lambda_Y X(t_a)}{\lambda_X-\lambda_Y}\times\left(\frac{e^{-\lambda_Y t_w}}{\lambda_Y}(1-e^{-\lambda_Y t_m})-\frac{e^{-\lambda_X t_w}}{\lambda_X}(1-e^{-\lambda_X t_m})\right).$$

The resulting activity at the end of irradiation, $X(t_a)$ or $Y(t_a)$, is determined via the induced γ activity. The number of decays during the subsequent measuring time t_m is

$$A_X=X(t_a)e^{-\lambda_X t_w}(1-e^{-\lambda_X t_m}), \tag{4}$$

where A_x are the number of decays, t_w the waiting time between irradiation and activity measurement, and t_a the activation time. The number of decays is referred from analysis of the characteristic lines in the measured γ-ray spectra,

$$A=\frac{CS_cK_{abs}}{I_\gamma\varepsilon_\gamma}, \tag{5}$$

where C are the number of counts per γ line, S_c the summing corrections, K_{abs} the correction for γ-self-absorption in the sample (negligible for the thin samples used in α activations), I_γ the line intensity per decay, and ε_γ the efficiency of the HPGe detectors. The γ-ray spectra were recorded and analyzed with the MPAWIN/4.0 system.

The γ-ray spectra showed prominent background lines from ^{43}K and ^{38}K due to ^{40}Ar$(\alpha,p)^{43}$K and ^{36}Ar$(\alpha,np)^{38}$K reactions. The strength of these lines being independent of the sample thickness indicates that argon had diffused into the tungsten backings during sputtering. Activation of the tungsten backings was not observed.

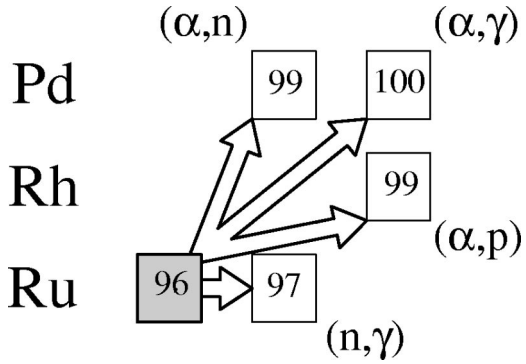

FIG. 6. The investigated reactions on ^{96}Ru. Note that the (α,n) channel contributes to the ^{99}Rh activity produced by (α,p) reactions.

TABLE III. Decay properties of the product nuclei.

Product nucleus	Reference		Half-life [23]	Gamma-ray energy (keV)	Relative intensity per decay (%)
^{100}Pd	[22]	Ground state	3.63±0.09 d	84.0	45.0±3.0
^{99}Pd	[22]	Ground state	21.4±0.2 min	136.0	72.7±1.6
^{99}Rh	[22]	Isomer	4.7±0.1 d	340.8	70.26±4.59
^{101}Pd	[22]	Ground state	8.47±0.06 h	296.3	19.2±1.0
^{97}Ru	[25]	Ground state	2.88±0.04 d	215.7	86.17±0.48
				324.6	10.24±0.39
^{103}Ru	[26]	Ground state	39.254±0.008 d	497.1	90.9±3.03
^{105}Ru	[27]	Ground state	4.44±0.02 h	262.8	6.58±0.21
				469.0	17.55±0.71
				676.4	15.66±0.64
				724.3	47.3±0.70

The γ-line intensities and half-lives listed in Table III were adopted from Refs. [22,23], respectively. The final uncertainties summarized in Table IV are less than 10% except at the lowest energies where counting statistics dominate.

B. Neutron-induced reactions

The (n,γ) cross sections were determined analogously to those of the α-induced reactions, except that the neutron flux was measured by means of the gold foils (Fig. 5). The time-integrated neutron flux Φ is

$$\Phi = \frac{CS_c}{I_\gamma \varepsilon_\gamma K_{abs}(1-e^{-\lambda_{\mathrm{Au}} t_m})e^{-\lambda_{\mathrm{Au}} t_w}\sigma_{\mathrm{Au}} N_{\mathrm{Au}} f_b} \qquad (6)$$

with most quantities being defined above. Here, the number of gold atoms in the sample is denoted by N_{Au} while the correction for decays during the activation is considered by the factor f_b (for a definition see Ref. [16]). The gold cross section averaged over the well-defined quasistellar spectrum is $\sigma_{25\ \mathrm{keV}}=(648\pm 10)$ mbarn [21].

The neutron flux was determined by the simultaneous irradiation of 0.03 mm thick gold foils on the front and back side of the Ru samples. The effective neutron fluxes were taken from the average of the respective gold activities. The uncertainty of the neutron flux determination originates essentially from the detector efficiency ε_γ ($\pm 2\%$) and from the gold cross section. The uncertainty related to the divergence of the neutron field was controlled by the activity differences of the two gold foils. The corresponding corrections were checked via the results obtained with the 0.2 and 1.0 mm thick Ru samples as well as by using samples of 6 mm, 8 mm, and 10 mm diameter. The related uncertainties were found to range between 0.1% and 0.5%. Additional uncertainties due to corrections for γ-ray self-absorption in the samples were comparably small. Based on the photoabsorption cross sections of Storm and Israel [24], these corrections were smaller than 7.0% and 1.5% for the thick and thin Ru samples, respectively. The corresponding uncertainties were well below 2%. Summing corrections due to coincident x rays were negligible because of the strong x-ray self-absorption in the comparably thick samples used for the (n,γ) studies.

The γ-line intensities per decay were adopted from Refs. [25–27], and the half-lives from Ref. [23]. The cross sections of ^{96,102,104}Ru were calculated according to Eq. (6) by changing index Au to Ru. The main contributions to the final uncertainties of 4–5 % are due to the neutron flux and the decay intensities (Table X).

V. RESULTS AND DISCUSSION

A. Reactions with α particles

Activation of the natural Ru samples provided a complete set of reaction cross sections for ^{96}Ru, i.e., ^{96}Ru$(\alpha,\gamma)^{100}$Pd from 7.0 to 10.6 MeV, ^{96}Ru$(\alpha,n)^{99}$Pd from 9.7 to 10.6 MeV, ^{96}Ru$(\alpha,p)^{99m}$Rh from 9.3 to 10.6 MeV, as well as the

TABLE IV. Uncertainties for FOR α-induced cross sections (in %).

Source of uncertainty	^{96}Ru(α,γ)	^{96}Ru(α,n)	^{96}Ru(α,p)	^{98}Ru(α,n)
Target thickness		3.5		
Efficiency of γ detectors		3.0		
Beam current measurement		1.0		
γ intensity per decay	6.7	2.2	6.5	5.2
Decay constants	2.5	0.9	2.1	0.7
Cascade corrections	2.0	0.5	<0.1	0.4
Counting statistics	<10.9	<2.1	<11.8	<13.4

TABLE V. Measured cross sections and S factors of the ^{96}Ru$(\alpha,\gamma)^{100}$Pd reaction.

Energy (MeV)	Cross section (μbarn)	S factor ($10^{24}\times$keV$\times$barn)
$10.556^{+0.024}_{-0.096}$	284 ± 32	$0.196^{+0.025}_{-0.026}$
$10.118^{+0.024}_{-0.047}$	188 ± 36	$0.382^{+0.074}_{-0.075}$
$10.118^{+0.024}_{-0.102}$	215 ± 25	$0.437^{+0.050}_{-0.051}$
$9.818^{+0.024}_{-0.100}$	232 ± 28	$1.03^{+0.12}_{-0.13}$
$9.715^{+0.024}_{-0.047}$	224 ± 27	$1.26^{+0.16}_{-0.16}$
$9.306^{+0.024}_{-0.103}$	167 ± 18	$3.10^{+0.34}_{-0.35}$
$9.023^{+0.024}_{-0.048}$	63 ± 7	$2.70^{+0.30}_{-0.31}$
$8.543^{+0.024}_{-0.068}$	28.6 ± 3.5	$5.60^{+0.68}_{-0.70}$
$8.159^{+0.024}_{-0.113}$	7.76 ± 0.82	$5.64^{+0.60}_{-0.61}$
$7.667^{+0.024}_{-0.151}$	1.92 ± 0.23	$8.67^{+1.03}_{-1.04}$
$7.029^{+0.024}_{-0.192}$	0.26 ± 0.04	$16.3^{+2.5}_{-2.6}$

^{98}Ru$(\alpha,n)^{101}$Pd cross section from 9.0 to 10.6 MeV. The results are summarized in Tables V–VIII, where asymmetric energy intervals indicate the ±24 keV uncertainty of the beam energy and the respective energy loss in the Ru layers.

^{96}Ru$(\alpha,\gamma)^{100}$Pd. Electron capture decay of ^{100}Pd feeds with 81% probability the 155.8 keV level in ^{100}Rh, followed by cascade transitions to the ground state. The (α,γ) cross section was evaluated via the strong 84 keV transition. Summing corrections of 26.2% and 26.6% due to the coincident detection of the accompanying cascade transitions were determined with the Monte Carlo code CASC [20]. Since ^{100}Pd decays via electron capture, additional summing corrections of 15% due to the coincident K_α and K_β x rays had to be considered as well. These corrections were deduced directly from the γ spectra as indicated in Fig. 7 and were therefore independent of detector efficiency and absorption effects in the sample and in the detector window. The resulting cross sections are presented in Table V. Comparison with theoretical predictions obtained with the statistical model code NON-SMOKER [28,29] in Fig. 9 shows fair agreement as far as the energy dependence is concerned, but the absolute values of the experimental data are two times smaller on average.

^{96}Ru$(\alpha,n)^{99}$Pd. The (α,n) channel opens at 9.56 MeV and was studied via the 136 keV γ transition populating the isomer of ^{99}Rh, since the decay branch to the ground state of ^{99}Rh is too weak to be detected. In this case γ-cascade corrections of 8.3% and 9.9% were calculated for the coincident

TABLE VI. Measured cross sections and S factors of the ^{96}Ru$(\alpha,n)^{99}$Pd reaction.

Energy (MeV)	Cross section (μbarn)	S factor ($10^{24}\times$keV$\times$barn)
$10.556^{+0.024}_{-0.096}$	1580 ± 130	$1.088^{+0.091}_{-0.098}$
$10.118^{+0.024}_{-0.047}$	569 ± 44	$1.159^{+0.093}_{-0.096}$
$10.118^{+0.024}_{-0.102}$	533 ± 40	$1.084^{+0.084}_{-0.092}$
$9.818^{+0.024}_{-0.100}$	234 ± 19	$1.043^{+0.0.087}_{-0.095}$
$9.715^{+0.024}_{-0.047}$	122 ± 9	$0.717^{+0.56}_{-0.058}$

TABLE VII. Measured cross sections and S factors of the ^{96}Ru$(\alpha,p)^{99m}$Rh reaction.

Energy (MeV)	Cross section (μbarn)	S factor ($10^{23}\times$keV$\times$barn)
$10.556^{+0.024}_{-0.096}$	1010 ± 190	7.0 ± 1.3
$10.118^{+0.024}_{-0.047}$	295 ± 74	6.0 ± 1.5
$10.118^{+0.024}_{-0.102}$	281 ± 67	5.7 ± 1.4
$9.818^{+0.024}_{-0.100}$	158 ± 34	7.0 ± 1.5
$9.306^{+0.024}_{-0.103}$	17.2 ± 3.5	3.19 ± 0.64

γ transitions, while the x-ray summing corrections of 7% were taken directly from the measured spectra as indicated in Fig. 8. Additional corrections of 4% due to coincidences between the 136 keV γ line and the 511 keV γ line from positron annihilation were also directly derived from the spectra. Two activations with different samples were carried out at 10.13 MeV α energy. The good agreement of both results confirms the procedures and corrections adopted in data analysis. The experimental data show again the predicted energy dependence of the NON-SMOKER calculations, but are smaller by an almost constant factor of three (see Fig. 9 and Table VI).

^{96}Ru$(\alpha,p)^{99m}$Rh. The product nucleus ^{99}Rh could only be detected via the short-lived isomer ($t_{1/2}=4.7$ h) because the activity related to the decay of the ground state ($t_{1/2}=16$ d) was too weak. There are no ground-state transitions from the isomer. The cross section was determined from the intensity of the 340 keV γ transition caused from an excited state of ^{99}Ru which is only populated from the ^{99}Rh isomer. The additional contribution to this isomer from the competing sequence ^{96}Ru$(\alpha,n)^{99}$Pd(electron capture decay)^{99}Rh had to be properly corrected since ^{99}Pd decays almost completely (97.9%) to the isomeric state of ^{99}Rh. The calculated cascade corrections were only 0.6% and 0.7%, respectively. The summing corrections due to x rays (10%) and due to the 511 keV annihilation line (1%) could be directly derived from the measured specta. No direct comparison with the theoretically predicted (α,p) cross section could be made because only the partial cross section had been determined in the experiment (Table VII). Nevertheless, it is interesting to note from Fig. 9 that the partial cross section exceeds the NON-SMOKER prediction for the *total* cross section [28,29] at

TABLE VIII. Measured cross sections and S factors of the ^{98}Ru$(\alpha,n)^{101}$Pd reaction.

Energy (MeV)	Cross section (μbarn)	S factor ($10^{24}\times$keV$\times$barn)
$10.565^{+0.024}_{-0.096}$	2680 ± 260	$1.84^{+0.18}_{-0.19}$
$10.126^{+0.024}_{-0.047}$	1410 ± 180	$2.89^{+0.36}_{-0.37}$
$10.126^{+0.024}_{-0.102}$	1400 ± 120	$2.85^{+0.25}_{-0.28}$
$9.826^{+0.024}_{-0.100}$	818 ± 91	$3.64^{+0.41}_{-0.44}$
$9.723^{+0.024}_{-0.048}$	460 ± 48	$2.71^{+0.29}_{-0.30}$
$9.313^{+0.024}_{-0.103}$	174 ± 29	$3.23^{+0.54}_{-0.57}$
$9.031^{+0.024}_{-0.048}$	81 ± 17	$3.48^{+0.72}_{-0.73}$

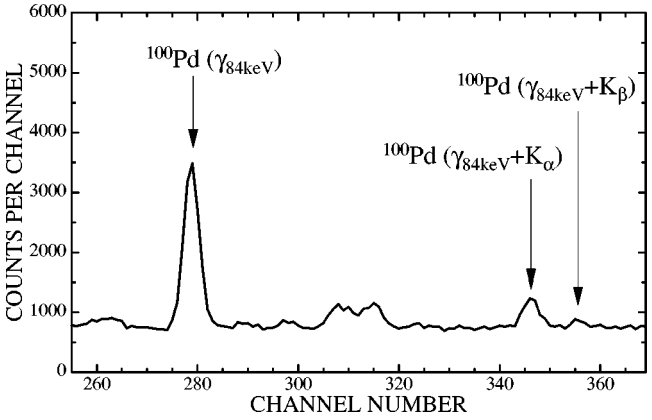

FIG. 7. The γ-ray spectrum after activation with an α beam of 9.7 MeV illustrating the (α,γ) channel. The 84 keV γ-ray line from the decay of ^{100}Pd and the corresponding line due to cascade summing with Rh x rays are marked by arrows.

energies above 10 MeV, in contrast to (α,γ) and (α,n) rates, which are systematically overestimated by the calculations.

^{98}Ru$(\alpha,n)^{101}$Pd. The use of natural Ru samples allowed to investigate the ^{98}Ru$(\alpha,n)^{101}$Pd reaction in the same experiment. The cross sections were deduced from the intensity of the 296.3 keV γ transition to the isomer state of ^{101}Rh (Table VIII). Summing corrections for cascade transitions (6.5% and 7.3%) and for x rays (18%) were determined as described before, while the corresponding effect due to 511 keV γ rays was found to be negligible in this case. Compared to the NON-SMOKER data [28,29] the measured (α,n) cross sections of ^{98}Ru are two times smaller on average (Fig. 9).

B. Neutron-induced reactions

The neutron activations resulted in stellar (n,γ) cross sections for ^{96}Ru, ^{102}Ru, and ^{104}Ru. As illustrated in Fig. 10 the γ-ray spectra of the activated Ru samples exhibit clear lines from all investigated reactions. The results obtained in the various activations are listed in Table IX. In all cases, the differences between individual activations are consistent

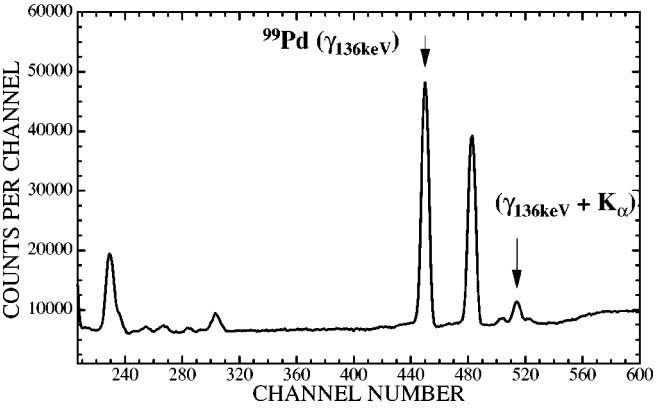

FIG. 8. The γ-ray spectrum after activation with an α beam of 10.5 MeV illustrating the (α,n) channel. The 136 keV γ-ray line from the decay of ^{99}Pd and the corresponding line due to cascade summing with Rh x rays are marked by arrows.

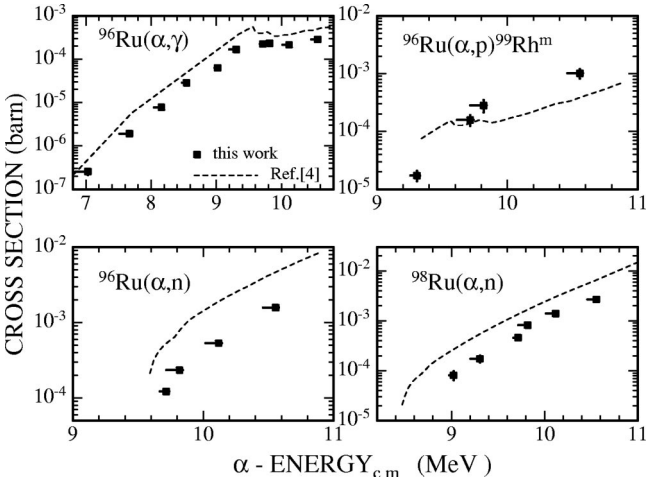

FIG. 9. The cross sections the α-induced reactions on ^{96}Ru and ^{98}Ru compared with the NON-SMOKER calculations (dashed lines). The asymmetric energy intervals indicate the 24 keV uncertainty of the beam energy and the energy loss in the Ru layers.

with the evaluated uncertainties (Table X). The present stellar cross sections are more accurate than previous values and help, therefore, to improve the reliability of these data at both ends of the long isotopic chain of Ru. This is important for comparison with data obtained in time-of-flight experiments, which are affected by completely different systematic uncertainties, as well as for testing statistical model predictions at the limits of stability.

^{96}Ru$(n,\gamma)^{97}$Ru. In this reaction the induced activity was evaluated from the γ lines at 215.7 keV and 324.6 keV. These strong lines allowed to check the systematic uncertainties related to the counting geometry by determining the induced activities with the 1 mm thick Ru samples placed at the standard distance of 73 mm as well as at a distance of 206 mm from the detector. The corresponding effect was smaller than 1% and compatible with counting statistics. Cascade corrections were always found to be smaller than 0.1%. The final stellar (n,γ) cross section of ^{96}Ru at $kT = 25$ keV is 229 ± 9 mbarn, in agreement but significantly more accurate than the currently recommended value of 263 ± 60 mbarn [30].

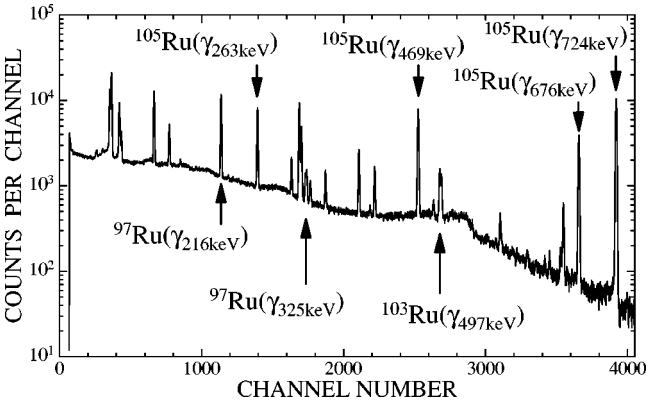

FIG. 10. The γ-ray spectrum after neutron activation of the Ru sample showing the lines for the various Ru isotopes.

TABLE IX. Measured stellar (n,γ) cross sections for $kT = 25$ keV thermal energy.

Sample thickness (mm)	Diameter (mm)	$\langle\sigma\rangle$ (mbarn) ^{96}Ru	^{102}Ru	^{104}Ru
1.0	6.0	227±9	166±8	178±9
	8.0	234±9	166±8	166±8
	10.0	225±9	166±8	175±9
0.2	6.0	236±10	169±8	166±9
	8.0	233±10	177±9	167±8
	10.0	220±10	165±9	159±8
Mean		229±9	169±8	169±8

^{102}Ru$(n,\gamma)^{103}$Ru. The induced ^{102}Ru activity was determined via the 497.1 keV γ transition. In this case, not only cascade corrections but also the correction for decays during the activation were negligibly small (<0.2%) because of the long ^{103}Ru half-life. Compared to the recommended value of 208±12 mbarn [30,31] the present result confirms that this cross section was severely overestimated in the past [32,33]. However, the present value of 169±9 mbarn is smaller by 23%, hardly compatible with the quoted uncertainties.

^{104}Ru$(n,\gamma)^{105}$Ru. The induced ^{105}Ru activity was detected using four γ transitions at 262.8, 469.0, 676.4, and 724.3 keV. Again, the consistent results obtained in counting the 1 mm thick samples at distances of 73 and 206 mm from the detector, confirmed the reliability of the sample-detector geometry as well as the cascade corrections, which were 2% for the shorter distance and negligible at 206 mm. The correction for the decay during activation was smaller than 10% in most cases. The present result of 169±8 mbarn is in good agreement with the previously recommended value of 180±10 mbarn [30].

The present results, which were determined for a thermal energy of $kT = 25$ keV, were extrapolated to higher and lower temperatures by normalizing the sets of recommended cross sections [30]. The results given in Table XI and the NON-SMOKER calculations agree on average within 30% at 30 keV. From the given comparison one might infer a trend to overestimate the actual cross section with decreasing neutron number in the theoretical calculations. When doing so one has to keep in mind that any trend might be masked or spuriously enhanced by the usual scatter in the predictions. Nevertheless, one may speculate that the NON-SMOKER neutron capture cross section might be overpredicted close to the $N = 50$ neutron shell closure. This is due to the underlying mass model [34] that enters into the calculation of the reaction Q values as well as into the calculation of the theoretical nuclear level densities. Following the approach of Ref. [35], a shifted Fermi-gas approach is used in NON-SMOKER to determine the level density at a given excitation energy, taking into account the thermal damping of shell effects. At very low energies, this is combined with the well-known constant temperature formula in order to obtain the correct behavior. The backshift is given by neutron-neutron and proton-proton pairing which is extracted from the utilized mass formula by mass differences. The second microscopic input to the level density description is the so-called microscopic correction that is used to compute the usual level density parameter a. This correction includes all effects going beyond a simple spherical droplet model and vanishes at high excitation energies. For the masses from the combined macroscopic-microscopic finite range droplet model (FRDM) used here, it conveniently is just the microscopic part of the mass formula as defined in Ref. [34]. Thus, microscopic information derived from the mass formula of choice enters in two ways into the level density, by the backshift and by the microscopic correction to the level density parameter. Therefore, switching to another mass model impacts the resulting cross-section predictions even when the Q values are unchanged because they are taken from experiment. On the other hand, it has been shown [35] that, as can be expected, deficiencies in the mass model translate into deviations of the predicted level densities with respect to experimental data, which in turn result in—much less pronounced, however—deviations in the reaction cross sections. The FRDM used here is known to show shell effects that are too strong, especially for the

TABLE XI. Stellar (n,γ) cross sections (in mbarn).

Thermal energy (keV)	^{96}Ru	^{102}Ru	^{104}Ru	
5	414±16	456±22	440±21	This work
10	342±13	297±14	291±14	This work
15	295±12	232±11	229±11	This work
20	258±10	194±9	193±9	This work
25	229±9	169±8	169±8	This work
30	207±8	151±7	151±7	This work
	281	147	100	NON-SMOKER [28,29]
40	175±7	127±6	128±6	This work
50	154±6	111±5	112±5	This work
60	138±5	98±5	100±5	This work
80	119±5	83±4	84±4	This work
100	108±4	72±3	74±4	This work

TABLE X. Uncertainties of the (n,γ) cross sections (in %).

Source of uncertainty	^{96}Ru(n,γ)	^{102}Ru(n,γ)	^{104}Ru(n,γ)
Efficiency of γ detector		2.0	
Neutron spectrum		<0.5	
Gold cross section		1.5	
Sample thickness		<0.4	
γ intensity per Au decay		0.1	
γ intensity per Ru decay	<0.7	<3.3	<2.5
Time-related uncertainties	<1.8	<0.3	<2.3
γ-ray self-absorption	<0.1	<0.1	<0.1
Cascade corrections	<0.1	<0.1	<0.1
Counting statistics	<0.9	<0.6	<0.8

$N=50$ shell [34]. This might be a source of increasing error in the theoretical capture cross sections when approaching shell closures. It should be noted that other mass models exhibit similar problems, even though with different magnitude (e.g., Refs. [29,35]). A few units away from the magic number, this effect should not be relevant anymore, though.

VI. SUMMARY

A series of cross-section measurements for α- and neutron-induced reactions on stable Ru isotopes has been carried out in the stellar energy regime. These data were intended to complement information from previous studies of (p,γ) reactions [12,13] in order to provide a set of experimental data for testing statistical model predictions relevant for *p*-process calculations. In this context, particular interest was put on the α-induced reactions because of the large discrepancy between theory and experiment reported for the ^{144}Sm(α,γ) cross section near the Gamov window of the *p* process [9].

The measured cross sections of the α-induced reactions confirm statistical model predictions with the NON-SMOKER code [28,29] to overestimate the experimental results systematically by a factor of 2.5. Similar discrepancies were also found in the (n,α) measurement of Ref. [11].

For the neutron reactions, consistent results were obtained in all six activations, independent of sample diameter and thickness. Compared to previous experiments, the ^{96}Ru cross section could be determined with seven times better accuracy. Theoretical and experimental (n,γ) cross sections agree within 30%, although the trend versus neutron number is considerably steeper in the calculated data.

Since also the Ru(p,γ) cross sections of Ref. [13] and the NON-SMOKER predictions agree within $\approx$60%, the present Ru results show that the theoretical treatment of the α channels is considerably more uncertain in the mass 100 region than the proton and neutron channels. This may indicate a general deficiency in the theoretical treatment of the α channels, although the observed discrepancies are less dramatic compared to the case of ^{144}Sm. Obviously, additional α-induced cross sections need to be measured over a wider mass range for understanding and improving this situation.

ACKNOWLEDGMENTS

We thank G. Rupp for his excellent technical support. For the RBS analyses we are indebted to G. Linker and R. Frommknecht, and for the XRF analyses to S. Rabung. The professional and engaged work of the accelerator teams, H. Eggestein, O. Röhr, M. Hoffmann at the cyclotron of PTB Braunschweig, and E-P. Knaetsch, D. Roller, W. Seith at the Karlsruhe Van de Graaff, are highly appreciated. This work was partially supported by the Swiss NSF (Grant No. 2000-061822.00). T.R. was supported by PROFIL (Swiss NSF Grant No. 2124-055832.98).

[1] S. Woosley and W. Howard, Astrophys. J. Suppl. **36**, 285 (1978).
[2] M. Rayet, M. Arnould, M. Hashimoto, N. Prantzos, and K. Nomoto, Astron. Astrophys. **298**, 517 (1995).
[3] W. Howard, B. Meyer, and S. Woosley, Astrophys. J. Lett. **373**, L5 (1991).
[4] V. Costa, M. Rayet, A. Zappalà, and M. Arnould, Astron. Astrophys. **358**, L67 (2000).
[5] M. Jaeger, R. Kunz, A. Mayer, J. W. Hammer, G. Staudt, K.-L. Kratz, and B. Pfeiffer, Phys. Rev. Lett. **87**, 201803 (2001).
[6] H. Schatz *et al.*, Phys. Rep. **294**, 167 (1998).
[7] H. Schatz, A. Aprahamian, V. Bernard, L. Bildsten, A. Cumming, M. Ouelette, T. Rauscher, F.-K. Thielemann, and M. Wiescher, Phys. Rev. Lett. **86**, 3471 (2001).
[8] Z. Fülöp, Á. Z. Kiss, E. Somorjai, C. Rolfs, H.-P. Trautvetter, T. Rauscher, and H. Oberhummer, Z. Phys. A **355**, 203 (1996).
[9] E. Somorjai, in *Nuclei in the Cosmos V*, edited by N. Prantzos and S. Harissopulos (Editions Frontières, Paris, 1998), p. 459.
[10] C. Grama and S. Goriely, in *Nuclei in the Cosmos V*, edited by N. Prantzos and S. Harissopulos (Editions Frontières, Paris, 1998), p. 463.
[11] Y. Gledenov, P. Koehler, J. Andrzejewski, K. H. Guber, and T. Rauscher, Phys. Rev. C **62**, 042801 (2000).
[12] T. Sauter and F. Käppeler, Phys. Rev. C **55**, 3127 (1997).
[13] J. Bork, H. Schatz, F. Käppeler, and T. Rauscher, Phys. Rev. C **58**, 524 (1998).
[14] W. Rapp, H. Brede, M. Heil, D. Hentschel, F. Käppeler, H. Klein, R. Reifarth, and T. Rauscher, Nucl. Phys. **A688**, 427c (2001).
[15] T. Rauscher and F.-K. Thielemann, in *Atomic and Nuclear Astrophysics*, edited by A. Mezzacappa (IOP, Bristol, 1998), p. 519.
[16] H. Beer and F. Käppeler, Phys. Rev. C **21**, 534 (1980).
[17] K. Toukan, K. Debus, F. Käppeler, and G. Reffo, Phys. Rev. C **51**, 1540 (1995).
[18] J. Ziegler, *Handbook of Stopping Cross-Sections for Energetic Ions in all Elements* (Pergamon Press, New York, 1980), Vol. 5.
[19] L. Doolittle, Nucl. Instrum. Methods Phys. Res. B **15**, 227 (1986).
[20] S. Jaag, Technical report, Kernforschungszentrum Karlsruhe (unpublished).
[21] W. Ratynski and F. Käppeler, Phys. Rev. C **37**, 595 (1988).
[22] R. Firestone, in *Table of Isotopes*, edited by V. Shirley (Wiley, New York, 1996).
[23] E. Browne and R. Firestone, *Table of Radioactive Isotopes* (Wiley, New York, 1986).
[24] E. Storm and H. Israel, Nucl. Data Tables **7**, 565 (1970).
[25] B. Haesner and P. Luksch, Nucl. Data Sheets **46**, 607 (1985).
[26] D. De Frenne, E. Jacobs, and M. Verboven, Nucl. Data Sheets **45**, 363 (1985).
[27] D. De Frenne, E. Jacobs, M. Verboven, and P. De Gelder, Nucl. Data Sheets **47**, 261 (1986).
[28] T. Rauscher and F.-K. Thielemann, At. Data Nucl. Data Tables **75**, 1 (2000).

[29] T. Rauscher and F.-K. Thielemann, At. Data Nucl. Data Tables **79**, 47 (2001).
[30] Z. Bao, H. Beer, F. Käppeler, F. Voss, K. Wisshak, and T. Rauscher, At. Data Nucl. Data Tables **76**, 70 (2000).
[31] R. Macklin and J. Halperin, Nucl. Sci. Eng. **74**, 174 (1980).
[32] B. Allen, J. Gibbons, and R. Macklin, Adv. Nucl. Phys. **4**, 205 (1971).
[33] M. Murty, K. Sidappa, and J. Rao, J. Phys. Soc. Jpn. **35**, 8 (1973).
[34] P. Möller, J. R. Nix, W. D. Myers, and W. J. Swiatecki, At. Data Nucl. Data Tables **59**, 185 (1995).
[35] T. Rauscher, F.-K. Thielemann, and K.-L. Kratz, Phys. Rev. C **56**, 1613 (1997).